Geomorphology 467 (2024) 109466

Contents lists available at ScienceDirect

Geomorphology

journal homepage: www.journals.elsevier.com/geomorphology

Oceanic geodiversity along back-arc spreading centers reveals analogies with mid-ocean ridges

C. Palmiotto [a,*], F. Muccini [b,c], E. Ficini [c], M.F. Loreto [a], M. Cuffaro [c]

[a] Cnr - Istituto di Scienze Marine, 40129 Bologna, Italy
[b] Istituto Nazionale di Geofisica e Vulcanologia, 00143 Roma, Italy
[c] Cnr - Istituto di Geologia Ambientale e Geoingegneria, 00185 Roma, Italy

ARTICLE INFO

Keywords:
Oceanic geodiversity
Back-arc spreading centers
Mid-ocean ridges
Bathy-morphological analysis
Plate kinematics

ABSTRACT

Oceanic geodiversity provides essential information on the dynamics of the Earth. Here, we focus on the geodiversity of three oceanic back-arc spreading centers: the Mariana Spreading Center, the Central-Southern Lau Basin spreading centers, and the East Scotia Ridge. We defined a method to identify their axial zones, obtaining spreading center depths along the basins. Results improve global plate boundary models and morphology variations, revealing that the average depths along the Mariana, East Scotia, and Lau Basin spreading ridges are 4.5, 3.5, and 2 km, respectively. We also measured new spreading rates based on five magnetic profiles crossing the three back-arc spreading centers, contributing to plate kinematic models. Furthermore, we computed subduction rates, including hinge velocities along the Mariana, South Sandwich, and Tonga Subductions, to understand the existing interactions between the subducting slab hinge motion and the kinematics of their related back-arc spreading centers. Our bathymetric, magnetic, and kinematic data show several differences among the Mariana, the East Scotia, and the Lau spreading centers, stressing the oceanic geodiversity in a similar geodynamic context. Our results also suggest a strong correlation between axial depth and full spreading rates along the back-arc spreading centers, a geological correspondence that allows a similar description of these divergent plate boundaries within the mid-ocean ridge classification. Finally, we show how hinge kinematics affects the relationship between convergence along subduction zones and back-arc spreading rates. All our findings contribute to understand how the oceanic geodiversity is directly related to geodynamic processes, increasing the knowledge of global tectonics.

1. Introduction

Geodiversity, i.e., the diversity of geological features in an area (Gray, 2004), allows quantifying geofeature variations across space or time (Tukiainen et al., 2023). If "on-land" geodiversity is catching on today, marine geodiversity is still in an embryonic stage, focused along coastal areas and/or submerged portions of islands (Maia and Castro, 2015). Although marine geodiversity provides essential information on the dynamics of the Earth, the geological diversity of the ocean floor, which makes up >70 % of the Earth's geodiversity, remains largely unexplored (Seijmonsbergen et al., 2022). Knowledge of marine geodiversity, resulting from geological processes such as tectonism, magmatic volcanism, sedimentary deposition, and modification by marine geomorphological processes, is crucial in understanding geological processes that operate in the marine domain.

This paper explores the "seafloor geodiversity" among zones where new oceanic crust forms in a similar geodynamic setting, i.e., the back-arc spreading centers (BASCs), within the back-arc basins (BABs) along convergent plate boundaries, and compares results with data along mid-ocean ridges (MORs), where new oceanic crust is created along divergent plate boundaries. According to the digital isochrons of the world's ocean floor (Müller et al., 1997), the global distribution of hydrothermal vent fields (Baker and German, 2004), and the first digital seafloor geomorphic features map of the global ocean (Harris et al., 2014), the class of "mid-ocean spreading ridges" includes all ridge–like features that coincide with the youngest ocean crust. However, processes of crustal accretion in back-arc regions, even if similar to those occurring on MORs (Taylor et al., 1996), are more complicated than those of the global MORs systems. Mechanisms that drive the upper plate extension and the formation of a mature oceanic spreading center along the BABs

* Corresponding author.
E-mail address: camilla.palmiotto@bo.ismar.cnr.it (C. Palmiotto).

https://doi.org/10.1016/j.geomorph.2024.109466
Received 10 May 2024; Received in revised form 18 October 2024; Accepted 19 October 2024
Available online 29 October 2024

are indeed linked to the different geological and geodynamic evolution of a single subduction system (Martinez and Taylor, 2002; Kato et al., 2003; Artemieva, 2023). Based on these considerations, BASCs were often excluded by the global system of MORs and not considered in the "spreading rates" classification by Dick et al. (2003) and reference therein, based on the velocity with which lithospheric plates diverge from each other (Vine and Matthews, 1963).

The main aim of this paper is to investigate morphological and kinematic characteristics and relationships between depth axis and spreading rates along different BASCs, improve bathymetric and magnetic data, and compare results with literature data along MORs in order to update the axial depth/full spreading rate correlation of Dick et al. (2003). Furthermore, we will show how the kinematic contribution strongly influences the spreading rates along BASCs, and how the evolution and diversity of subductions strongly affect the extension along oceanic back-arc basins. We thus considered three different spreading centers formed along different oceanic back-arc basins: (1) the Mariana Spreading Center (MSC) in the Pacific Ocean, along the Mariana Trough (Fig. 1); (2) the East Scotia Ridge (ESR) along the East Scotia Sea BAB in the Atlantic Ocean (Fig. 1); (3) spreading centers along the Central-Southern part of the Lau Basin (CSLB) in the Pacific Ocean (Fig. 1). The MSC, the ESR, and the CSLB, formed in a similar geodynamic setting of ocean-ocean subduction (Larter and Leat, 2003; Artemieva, 2023), provide a good tectonic laboratory to study and compare marine geodiversity and better understand ocean floor dynamics along spreading ridges. These three areas have been chosen because they are mature spreading centers related to the opening of back-arc basins, whereas others are in their closing stage, or their development is related to additional tectonic processes other than slab retreat (i.e., the accommodation of different upper plate velocities; see Doglioni et al., 2007 and references therein).

We used: (1) bathymetric datasets to create regional maps in order to identify in detail the axis along the three BASCs and refine a large part of microplate-plate boundaries in those areas (Bird, 2003; Cuffaro and Jurdy, 2006; DeMets et al., 2010); (2) five magnetic profiles located along the central parts of the MSC, ESR, and CSLB, to compute the related spreading rates and improve the literature; (3) a kinematic model, which takes into account subduction rates (i.e., the effective velocity at which the tip of a subducting plate enters the mantle; Ficini et al., 2020) along the Mariana, South Sandwich, and Tonga Subductions to investigate the relationship between spreading rates along the BABs and understand which parameter plays the major role in determining the morphology of the BASCs.

2. Geodynamic settings

2.1. Mariana Trough

The Mariana Trough (MT), located between ~12° and 22° N in the Pacific Ocean, is a back-arc basin formed by extensional tectonics due to the subduction of the Pacific below the Philippine plate along the Mariana Subduction (MS; Fig. 2a; Artemieva, 2023 and reference therein). The Mariana Spreading Center (MSC), located within the isochrones of 2 Ma in Fig. 2b, lies in the center of the trough, between the West Mariana Ridge (WMR) and the Volcanic Mariana Arc (MVA; Fig. 2a). The first studies on seafloor spreading along the MSC were published in the early '70s by (Karig, 1971; Anderson, 1975), and after the IODP expeditions (Karig et al., 1978; Hynes and Mott, 1985; Yamazaki et al., 1993; Martinez et al., 1995; Kato et al., 2003). In recent years, with multibeam, submersible studies, and modern technology (i.e., Autonomous Underwater Vehicles and Remotely Operated Underwater Vehicles), portions of the central and southern MSC have been studied in detail (Fujiwara et al., 2008; Anderson et al., 2017; Chadwick Jr et al., 2018).

The MT is ~1300 km and ranges between 3 and 6 km in depth; its width changes from 220 km in the southern zone to 0 in the northern region, where the inactive and active volcanic arcs meet (Fig. 2a). Major seismic activity is observed along the southern and central zones of the basin; focal mechanisms show extensive tectonics along the MSC (Fig. 2a). The dip of the Mariana slab, here computed by fitting the location of the hypocenters in a longitude/depth diagram (Fig. 2a), shows that it ranges from 56° in the north (profile 1) to 77° in the center (profile 2) and to 55° in the south (profile 3). The depth of the hypocenters is >300 km only in the central region, where the slab is steeper. The age of the subducting oceanic crust (Fig. 2b) ranges from 140 to 154 Ma (Müller et al., 2019; Seton et al., 2020); otherwise, the oceanic crust along the MSC is very young: according to Yan et al. (2022), rifting began <10 Ma, whereas the spreading stage forming new oceanic crust started only ~4 Ma (Bibee et al., 1980). According to the plate kinematic models of DeMets et al. (2010), the convergence rates along the Mariana Subduction decrease southward, from 27 mm/a in the central part to 19 mm/a to the south (Fig. 2b); the direction of motion of the lower plate (black arrows in Fig. 2b) is oblique to the subduction trend.

2.2. East Scotia Sea Back-Arc Basin

The East Scotia Sea BAB (Fig. 3), located between ~55° and 60° S,

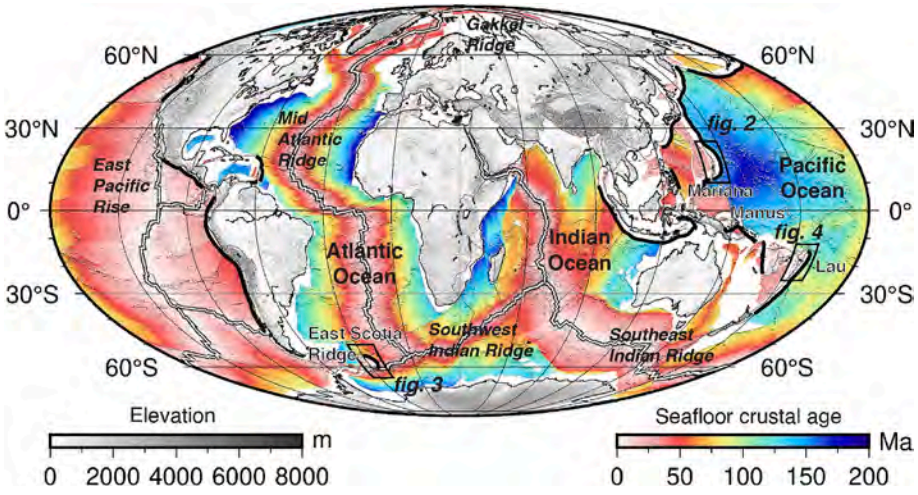

Fig. 1. Global distribution of mid-ocean ridges (white solid line) and subduction zones (black solid line). Topography and seafloor crustal age are from 1-minute resolution GEBCO database (General Bathymetric Chart of the Oceans), whereas the global dataset of oceanic crustal age is by Müller et al. (2019) and Seton et al. (2020). Plate boundaries (black thin line) have been plotted using data by DeMets et al. (2010). Black boxes indicate the area analyzed in this paper.

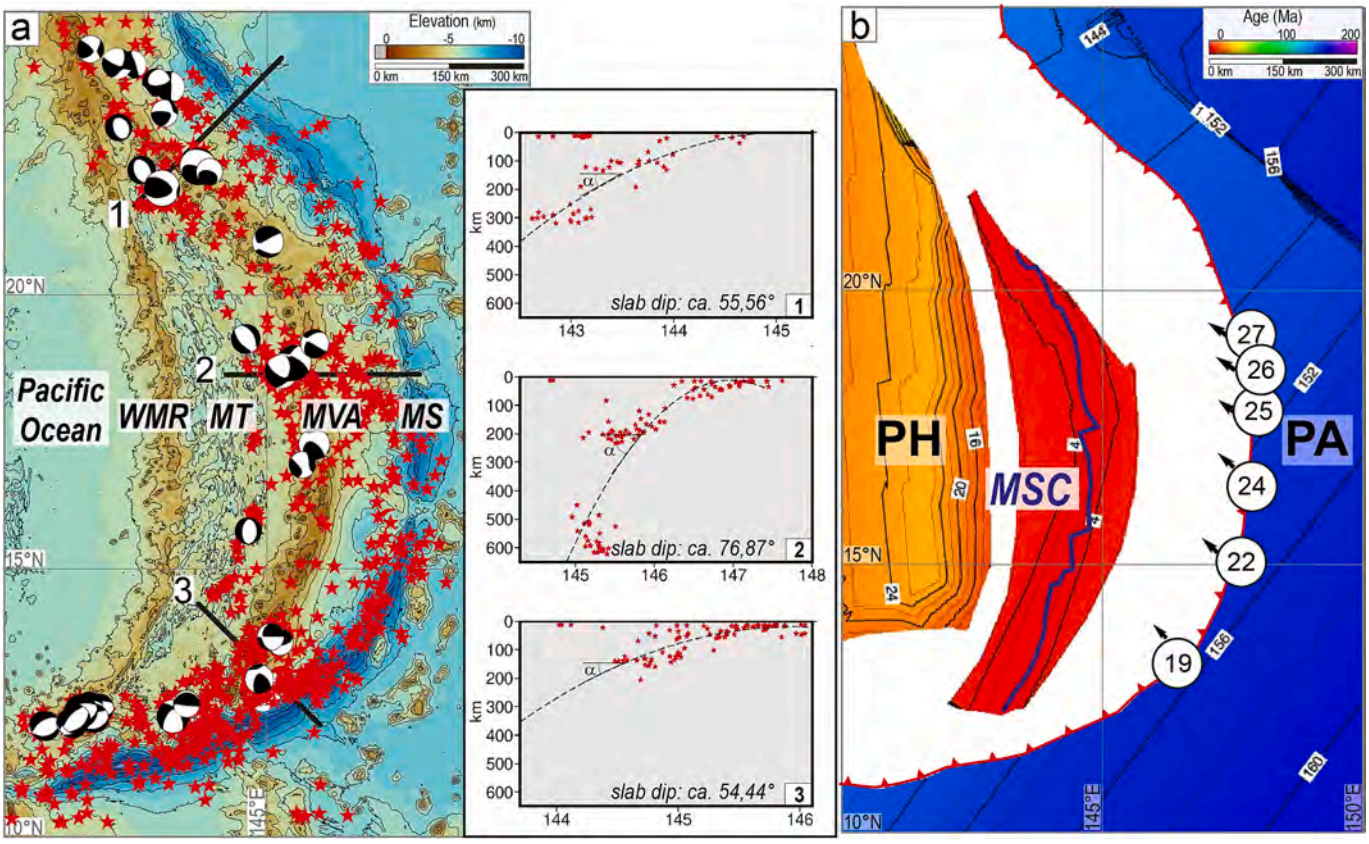

Fig. 2. a) Shaded regional bathymetric map of the Mariana Trough from the GEBCO database (GEBCO_2023GRID; https://download.gebco.net/). WMR: West Mariana Ridge; MT: Mariana Trough; MVA: Mariana Arc; MS: Mariana Subduction. Red stars: earthquakes. Distributions of earthquakes and focal mechanisms are from the USGS database archives (http://earthquake.usgs.gov/) and from the CMT catalog (Ekstrom et al., 2012). Black solid lines 1, 2, and 3 show the dip of the slab relative to the northern, central, and southern parts of the Mariana Subduction (three diagrams on the right). Scientific color maps used are based on Crameri et al. (2020). b) Age of oceanic crust image along the Mariana region. Solid-black lines are isochrones obtained using data by Müller et al. (2019) and Seton et al. (2020). According to DeMets et al. (2010), the red line with triangles is the Mariana subduction and the blue line is the Mariana Spreading Center (MSC). White circles show the convergent velocity (V_L) in mm/a, estimated for each point using the MORVEL plate kinematic models by DeMets et al. (2010). Black arrows show the direction and the motion of the lower plates. PA: Pacific plate; PH: Philippine plate.

formed by the subduction of Sur below the Sandwich plate (DeMets et al., 2010). The East Scotia Ridge (ESR), lies in the center of the basin for ~650 km, west of the Sandwich Arc (SA) and of the South Sandwich Subduction (SSS) (Fig. 3a). Bathymetry, petrogenesis, magnetic, and spreading data of the ESR have been studied by Fretzdorff et al. (2002) and references therein, Taylor and Martinez (2003), Leat et al. (2004), and Smalley Jr. et al. (2007). Major seismic activity is located along the SSS and along the southern and northern parts of the East Scotia Sea BAB, where focal mechanisms show extensional and transcurrent tectonics (Fig. 3a). The dip of the slab is here computed (Fig. 3a): it ranges from 40° in the northern region (profile 1) to 55° in the center (profile 2) and 49° in the southern region (profile 3). The depth of the hypocenters along the Sandwich slab is <300 km in all the region. The age of the oceanic crust of the Sur subducting plate ranges from 50 to 80 Ma along the northern part of the trench, and from 8 to 30 along the Southern region (Müller et al., 2019; Seton et al., 2020); the age of the oceanic crust along the ESR is ~8 Ma (Fig. 3b). According to the plate rotation model by DeMets et al. (2010), convergence rates along the SSS increase southward, from 66 mm/a in the northern part to 77 mm/a to the south (Fig. 3b); the direction of motion of the lower plate (black arrows in Fig. 3b) is mostly perpendicular to the subduction trend.

2.3. Central-Southern Lau Back-Arc Basin

The Lau BAB results from the subduction of the Pacific plate under the Australian plate (Fig. 4; Karig, 1970; Malahoff et al., 1982; Hynes and Mott, 1985; Parson and Wright, 1996; Martinez and Taylor, 2002). It is located between ~14° and 24° S in the Pacific Ocean and is characterized by a triangular shape >1000 km long, ranging in width from 450 km in the north to 200 km in the south. In this paper, we only focus on the spreading centers along the Central-Southern part of the Lau Basin (CSLB), west of the Tonga Ridge (TR), leaving out the northern part of the Lau Basin (Fig. 4a), as it was discussed in Palmiotto et al. (2022) and references therein. Major seismic activity is observed in the northern part of the Lau Basin (NLB) and along the TS; focal mechanisms show transcurrent tectonics along the NLB and the CSLB (Fig. 4a). The dip of the Tonga slab (Fig. 4a), ranges from 45° in the north (profile 1) to 57° in the center (profile 2) and to 59° in the south (profile 3). The subducting oceanic crust (Fig. 4b) ranges from 122 Ma in the northern part to 88 Ma in the southern part (Müller et al., 2019; Seton et al., 2020). According to plate velocities derived by DeMets et al. (2010), convergence rates along the TS decrease southward, from 216 mm/a in the northern part to 204 mm/a to the south (Fig. 4b); the direction of motion of the lower plate (black arrows in Fig. 4b) is mostly perpendicular to the trend of the subduction.

3. Data and methods

3.1. Bathymetry, seismicity, and age of crust data

Global elevation in Fig. 1 is from the 1-minute resolution GEBCO database (General Bathymetric Chart of the Oceans); the global dataset

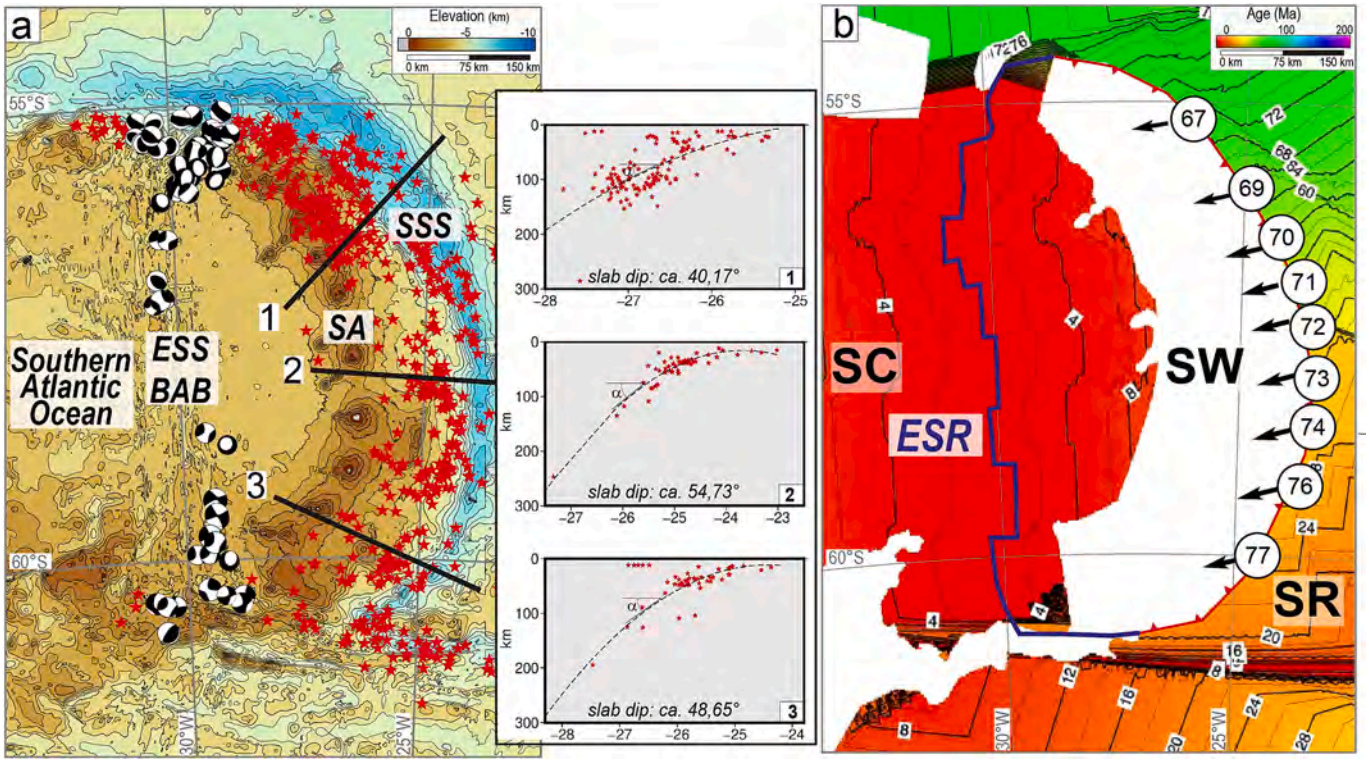

Fig. 3. a) Shaded regional bathymetric map of the East Scotia Sea Back-Arc Basin and of the South Sandwich Subduction in the Southern Atlantic Ocean; data are from the GEBCO database (GEBCO_2023GRID; https://download.gebco.net/) and from the site of the British Antarctic Survey (https://data.bas.ac.uk/metadata.php?id=GB/NERC/BAS/PDC/00812). Red stars: earthquakes. Distributions of earthquakes and focal mechanisms are from the USGS database archives (http://earthquake.usgs.gov/) and from the CMT catalog (Ekstrom et al., 2012). Black solid lines 1, 2, and 3 show the dip of the slab relative to the northern, central and the southern part of the South Sandwich Subduction (three diagrams on the right). The scientific color maps used are based on Crameri et al. (2020). ESS BAB: East Scotia Sea Back-Arc Basin; SA: Sandwich Arc; SSS: South Sandwich Subduction. b) Age of oceanic crust images along the East Scotia Sea region. Solid-black lines are isochrones obtained using data by Müller et al. (2019) and Seton et al. (2020). According to DeMets et al. (2010), the red line with triangles is the South Sandwich subduction and the blue line is the East Scotia Ridge (ESR). White circles show the convergent velocity (V_L) in mm/a, estimated for each point using the MORVEL plate kinematic models by DeMets et al. (2010). Black arrows show the direction and the motion of the lower plates. SW: Sandwich plate; SR: Sur plate.

of oceanic crustal age in Figs. 1, 2b, 3b, 4b, and 8 is by Müller et al. (2019) and Seton et al. (2020). The bathymetry of the Mariana, East Scotia Sea, and the Central-Southern Lau BAB regions (Figs. 2–7 and Supplementary Figures) were modeled using grid data with a 15 arc-second resolution downloaded from the GEBCO website. The bathymetry of the East Scotia Sea BAB has been merged with the bathymetric and topographic compilation of the South Sandwich Island Volcanic Arc available from the site of the British Antarctic Survey (https://data.bas.ac.uk/metadata.php?id=GB/NERC/BAS/PDC/00812; Fretwell, 2015). The Global Mapper Software was used for spatial analysis, to create 2D digital elevation images and perform the bathy-morphological analysis along the MSC and ESR. The Minitab Software was used to plot the results of the bathymetric, magnetic, and kinematics analysis in diagrams.

Distributions of earthquakes and focal mechanisms are from the USGS database archives (http://earthquake.usgs.gov/) and from the CMT catalog (Ekstrom et al., 2012). Spatial analysis and mapping were performed using the Generic Mapping Tools open-source software (Wessel et al., 2019).

3.2. Axial zone definition methods

We propose a method to identify the axial zone along back-arc spreading centers. First, we made 100 km long bathymetric profiles perpendicular to the trend of each ridge segment. Along the Mariana Spreading Centers (MSC; ~1000 km of length), we made a bathymetric profile at each 10 km; along the East Scotia Ridge (ESR; ~500 km of length), each 5 km; finally, along the spreading centers in the Central and Southern part of the Lau Basin (CSLB; ~700 km of length), each 7 km. We then interpreted each single bathymetric profile and identified the axial zone based on the following rules: 1) in the case of a morphological rise, the axial point corresponds to the highest part along the segment; 2) in the case of a symmetric valley, the point corresponds to the deepest part along the segment; 3) in the case of a symmetric valley characterized by several volcanoes, we fixed the point in the active volcanic part of the segment; 4) in the case of an asymmetric valley, we considered the width of the axial zone, or the length between the western and the eastern flanks and fixed the axial point halfway. We fixed 111 points along the MSC and the ESR, and 86 points along the segments of the CSLB, obtaining the depth variations along their axial zone. After this operation, we made a 60 km long bathymetric profiles perpendicular to the ridge segments (30 km along the eastern flank and 30 km along the western flank), obtaining the variation of morphology along the BASCs. We decided to analyze only the first 30 km because in several cases, beyond 30 km, we fall out of the back-arc basin, crossing the active volcanic arc. The location of all derived axial points and the 60-km bathymetric profiles are reported in the Supplementary Figures and Materials. We estimated axial point localization uncertainties in the order of 10 km, corresponding to the highest width detected in the analyzed symmetric and asymmetric rift valleys along the three back-arc spreading centers. Lower uncertainties, in the order of 4 km, can be obtained when investigating spreading ridges with rises instead of valleys.

3.3. Magnetics

We used five selected magnetic track lines available from the Marine

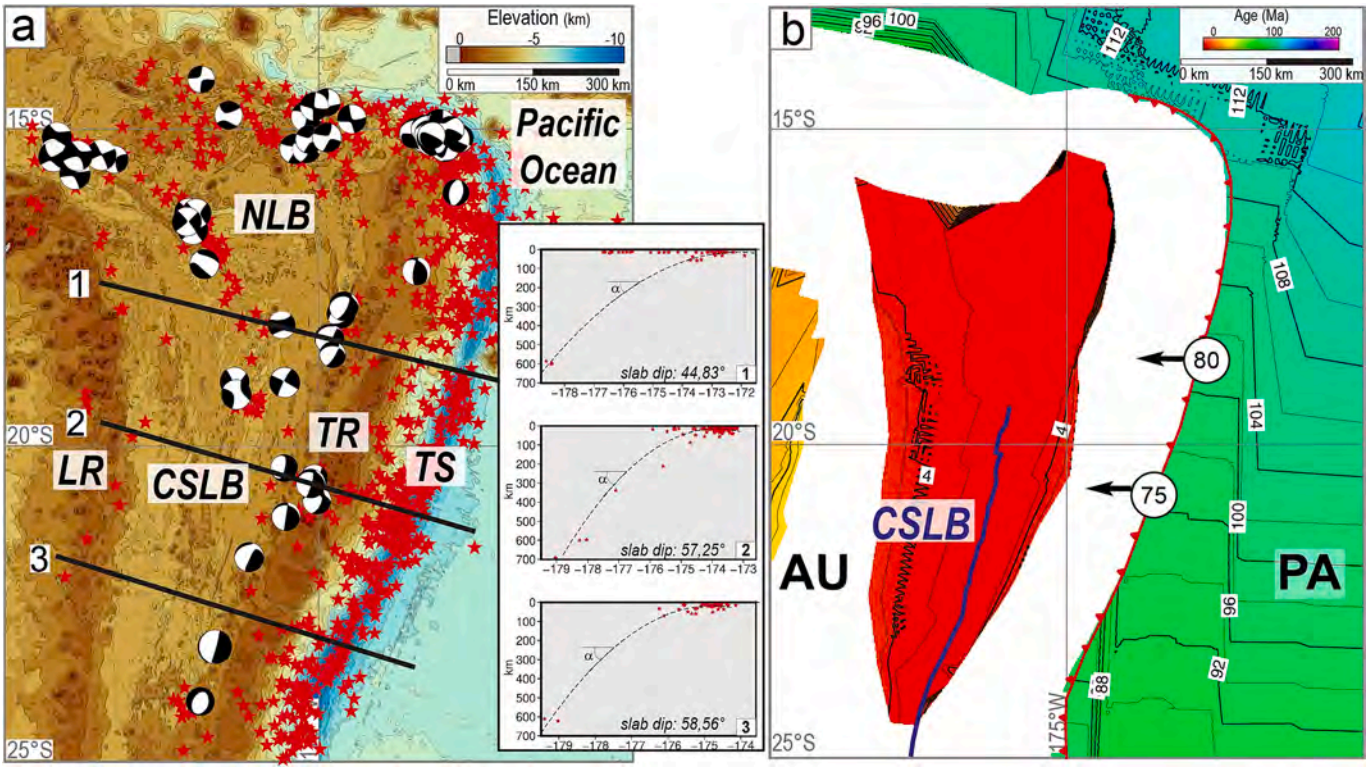

Fig. 4. a) Shaded regional bathymetric map of the Lau Basin Back-Arc Basin and of the Tonga in the Pacific Ocean; data from the GEBCO database (GEBCO_2023GRID; https://download.gebco.net/). Red stars: earthquakes. Distributions of earthquakes and focal mechanisms are from the USGS database archives (http://earthquake.usgs.gov/) and from the CMT catalog (Ekstrom et al., 2012). The black solid lines 1, 2, and 3 show the dip of the slab relative to the northern, central, and southern part of the Tonga Subduction (three diagrams on the right). The scientific color maps used are based on Crameri et al. (2020). NLB: Northern Lau Basin; CSLB: Central-Southern Lau Basin; LR: Lau Ridge; TR: Tonga Ridge; TS: Tonga Subduction. b) Age of oceanic crust images along the Central-Southern Lau Basin region. The black-solid lines are isochrones obtained using data by Müller et al. (2019) and Seton et al. (2020). According to DeMets et al. (2010), the red line with triangles is the Tonga Subduction and the blue line is the spreading center in the Central-Southern Lau Basin (CSLB). White circles show the convergent velocity (V_L) in mm/a, estimated for each point using the MORVEL plate kinematic models by DeMets et al., 2010. Black arrows show the direction and the motion of the lower plates. PA: Pacific plate; AU: Australia plate.

Trackline Geophysical Data (NOAA, 1977). We calculated the magnetic anomalies from the line of the surveys TUNE07WT (Mariana Spreading Center), CD37_889 and ODP113JR (East Scotia Ridge), RNDB15W, and MW9603 (Central-Southern Lau Basin). Raw data acquisition spans over 12 years (from 1987 to 1999). Total field magnetic anomalies were calculated by removing the International Geomagnetic Reference Field (IGRF-12 model; Thébault et al., 2015). These anomalies were used to obtain the average full spreading rate following the approach proposed by Mendel et al. (2005) and based on the geomagnetic polarity time scale of Cande and Kent (1995). A magnetization intensity of 10 A/m on the axis and 5 A/m off the axis, respectively, and a constant source layer thickness of 0.5 km were assumed in the modeling; declination and inclination derived from the calculated IGRF model. We restricted the full spreading rate estimation to the last 2.58 Ma in the Mariana and South Sandwich back-arc basin areas and to the last 0.78 ma and 1.77 Ma in the Lau Basin region, because these intervals allow a good relationship between magnetic anomalies and relative chronos.

3.4. Kinematic model

Computing the subduction rate allows us to evaluate the effective velocity with which the tip of a subducting plate enters the mantle. Differently, the convergence velocity gives the velocity with which a moving plate approaches the trench before subducting. Between these two final values, the subduction hinge motion (V_H) holds the leading role. This feature represents the point of maximum curvature on a subducting slab, and its kinematics are crucial to understanding the dynamics of a subducting slab. The difference between the convergence rate (V_L) and the subduction rate lies in the behavior of the slab hinge relative to the upper plate; in particular, the hinge can move away or toward the fixed upper plate (Doglioni et al., 2006). Following the approach of Ficini et al. (2020), we used the relation (1) to compute the subduction rate V_S (Doglioni et al., 2007):

$$V_S = V_H - V_L, \quad (1)$$

where V_L was estimated for each point using the MORVEL current plate motion models (DeMets et al., 2010), and V_H was evaluated starting from available GPS data:

i) from Kato et al. (2003) for the Mariana Subduction zone;
ii) from Smalley Jr. et al. (2007) and Ficini et al. (2020) for the South Sandwich Subduction zone, computing the residual velocity with respect to the Sandwich plate (MORVEL current plate kinematics models; DeMets et al., 2010);
iii) from Ribeiro et al. (2017) for the Tonga Subduction zone.

4. Results

4.1. Mariana Spreading Center

Based on the bathymetric analysis, we obtained that the MSC can be described with nine main segments from north (MSC1; red points) to south (MSC9; grey points) (Fig. 5a). We plotted the trend of the MSC axial depth relative to latitude in Fig. 5b (blue solid line in the diagram depth/latitude); the location and depth of each point fixed along the

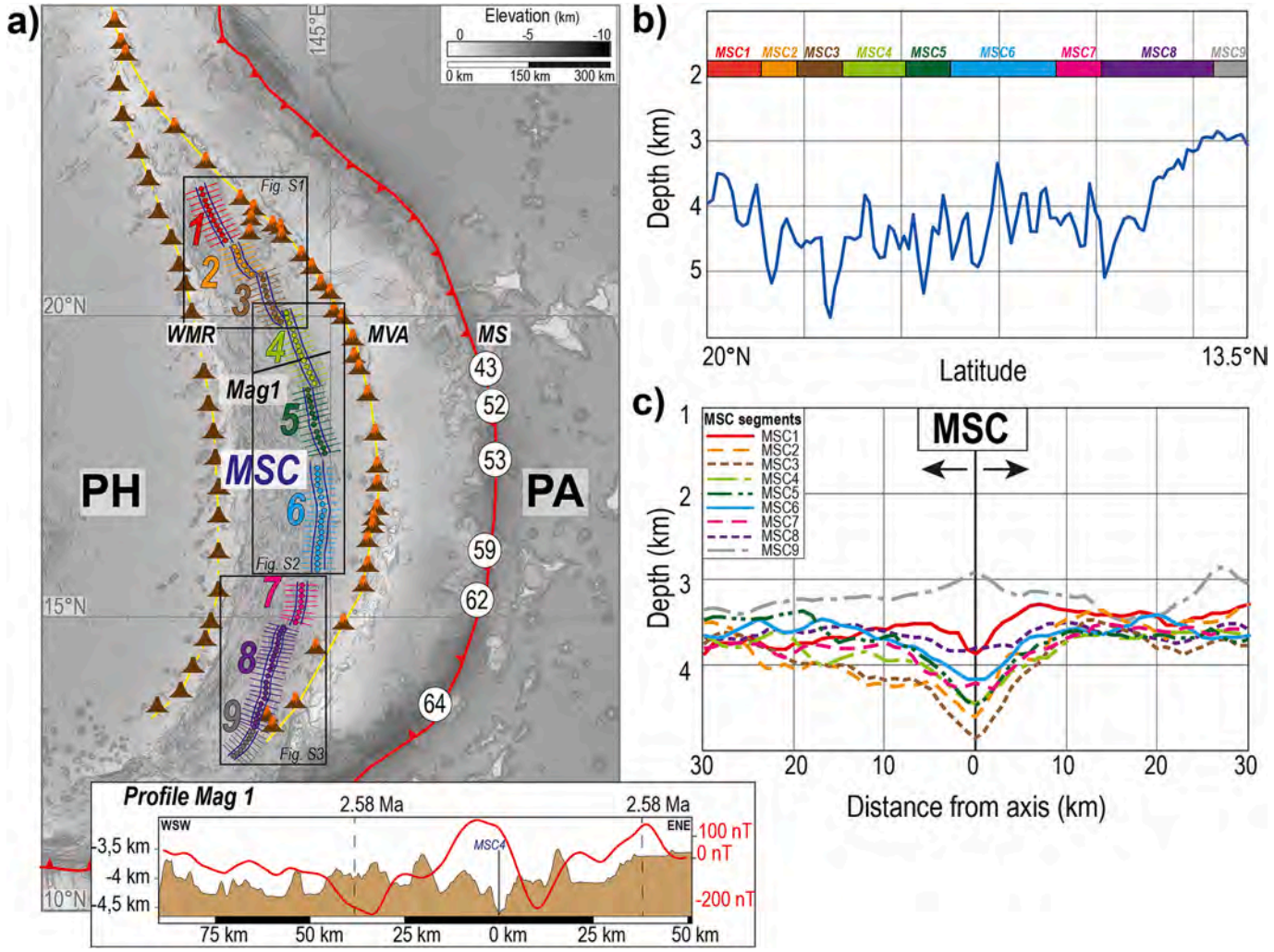

Fig. 5. a) Shaded grey relief image of the Mariana region. Colored dots and lines are respectively the 111 points and the bathymetric profiles identified and analyzed along the Mariana Spreading Center (MSC). Red dots and lines: MSC segment 1; Orange dots and lines: MSC segment 2; Brown dots and lines: MSC segment 3; Light green dots and lines: MSC segment 4; Dark green dots and lines: MSC segment 5; Light blue dots and lines: MSC segment 6; Pink dots and lines: MSC segment 7; Purple dots and lines: MSC segment 8; Light grey dots and lines: MSC segment 9. The blue solid lines show the trend of the spreading segments. The black solid line crossing the MSC segment 4 is the bathymetric and magnetic profile Mag1 shown in the lower part of the figure. White circles show the subduction rate (V_S) in mm/a measured according to Ficini et al. (2020). WMR: West Mariana Ridge; MT: Mariana Trough; MA: Mariana Arc; MS: Mariana Subduction. The dashed-yellow line and brown triangles show the extinct volcanism of the WMR; the solid-yellow line and brown-orange triangles show active volcanism of the MA; the solid-red line with red triangle show the MS. b) The blue solid line in the diagram on the right shows the variation of the axial depth along the MSC from north (20°N of latitude) to south (13.5°N of latitude). c) Depth/Distance from the axis diagram. Each profile represents an average of all bathymetric profiles obtained along each segment. The axis of the MSC is in correspondence of the 0 km in the lower part of the diagram; the right parts of the profiles reflect the eastern flanks of the MSC; the left parts of the profiles reflect the western flanks of the MSC.

MSC are shown in Figs. S1, S2, and S3. The northern part of the region is the deepest part of the basin: here, the depth of the axis ranges between 4 and 5,6 km below sea level, with a maximum value of −5.695 km at ~20°N, along the third segment. The axial depth range between 4 and 5 km below sea level in the central part (segments from 4 to 8), except for a few points that reach −3.5 km depth. The southern part of the MSC is the shallowest region: here, the axial depth along the southern part of segment 8; along the MSC9, is <3.5 km, reaching the minimum depth of 2.8 km at ~13°N. The length of segments ranges from a minimum of 60 km (MSC2) to a maximum of 200 km (MSC8). The MSC's trend changes from NW-SE (segments from MSC1 to MSC5) to N-S in the central area (MSC6) and NE-SW in the southern zone (from MSC7 to MSC9), similar to the Mariana Subduction trend (Fig. 5a). Based on the investigation of 111 60-km-long bathymetric profiles perpendicular to the MSC axis (Figs. 5a and S4 to S12), we obtained the mean range of depth for each segment (Fig. 5c), which implies the variation of morphology of the first 30 km along the axis of the MSC. Segments from MSC1 to MSC6 (Fig. 5c) are characterized by an axial valley flanked by steep walls. The depth of the valley ranges from ~3.5 to ~5.6 km; this is the deepest part along the entire MSC. Segments from MSC4 to MSC8 show a shallower valley, with depths ranging from 5 to 4 km and width from 5 to 20 km. The MSC9, in the southern region, is the only segment characterized by an axial high at ~3 km of depth (Fig. 5c). Based on magnetic data, we estimated a full spreading rate of 23,6 mm/a along the MSC4 (Fig. 5a). The correlation between the magnetic and bathymetric profiles shows an asymmetry in seafloor spreading: the western flank of the MCS is significantly faster than the eastern one. The subduction rate calculated along the MS, shown in the white circles along the red solid line in Fig. 5a, increases from the central part (~43 mm/a) to the south (~64 mm/a).

4.2. East Scotia Ridge

Similar to MSC, our analysis suggests that the ESR can be divided into

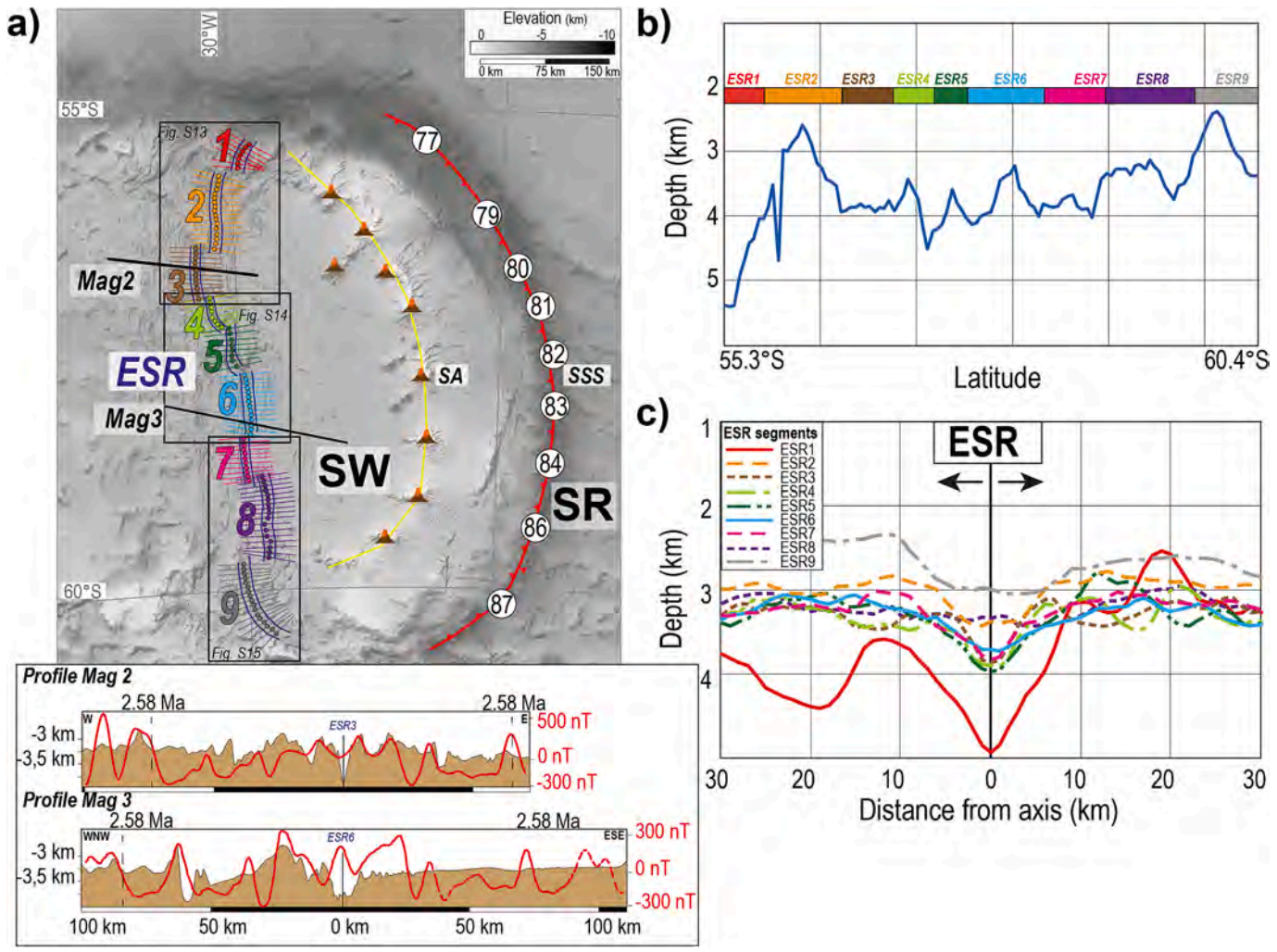

Fig. 6. a) Shaded grey relief image of the East Scotia Sea region. Colored dots and lines are respectively the 111 points and the bathymetric profiles identified and analyzed along the East Scotia Ridge (ESR). Red dots and lines: ESR segment 1; Orange dots and lines: ESR segment 2; Brown dots and lines: ESR segment 3; Light green dots and lines: ESR segment 4; Dark green dots and lines: ESR segment 5; Light blue dots and lines: ESR segment 6; Pink dots and lines: ESR segment 7; Purple dots and lines: ESR segment 8; Light grey dots and lines: ESR segment 9. Blue solid lines show the trend of the spreading segments. Black solid lines crossing the ESR segments 3 and 6 represent the bathymetric and magnetic profiles Mag2 and Mag3 shown in the lower part of the figure. White circles show the subduction rate (V_S) in mm/a measured according to Ficini et al. (2020). ESR: East Scotia Ridge; SA: Sandwich Arc; SSS: South Sandwich Subduction. The solid-yellow line and brown-orange triangles show active volcanism along the SA; the solid-red line with red triangles shows the SSS. b) The blue-solid line in the diagram on the right shows the variation of the axial depth along the ESR from north (55.3°S of latitude) to south (60.4°S of latitude). c) Depth/Distance from the axis diagram. Each profile represents an average of all bathymetric profiles obtained along each segment. The axis of the ESR is in correspondence of the 0 km in the lower part of the diagram; right parts of the profiles reflect the eastern flanks of the ESR; left parts of the profiles reflect the western flanks of the ESR.

nine main segments from north (ESR1; red dots) to south (ESR9; grey dots) (Fig. 6a). We plotted the points in the depth/latitude diagram of Fig. 6b obtaining the trend of the ESR axial depth from the northern to the southern basin; the location and depth of each point fixed along the ESR are shown in Figs. S13, S14, and S15. Results show that: a) the maximum axial depth along the ESR is along the first part of the first segment (5.392 km at ~55.3°S), in the Northern East Scotia Sea basin; b) from the beginning of segment 3 to the end of segment 8, the ESR axial depth ranges from 4.3 and 3 km below sea level; c) the axial depth along the second and the last segment is <3 km, reaching a minimum of 2.595 km along the ESR2 and 2.389 km along the ESR9. The lengths of the nine ESR segments range from 40 to 100 km, and the trend is from NNW-SSE (northern region) to NNE-SSW (southern region). With the analysis of the 111 60-km-long bathymetric profiles perpendicular to the ESR axis (Figs. 6a and S16 to S24), we show the variations of morphology along ESR segments. The mean range of depth for each segment, showing the variation of morphology of the first 30 km along the axis of the ESR, is shown in Fig. 6c and in the Supplementary Materials. The bathymetry of segments ESR1 and ESR3 shows a deep (−4 km) and narrow (width < 10 km) median valley flanked by steep walls; the segment in between, the ESR2, is shallower (~−3 km), and it shows neither a valley nor a rise. Segments from 4 to 8 are all characterized by a median axial valley ranging from 4 to 3 km of depth and from 10 to 20 km in width. The southern segment, the ESR9, is the only one to be characterized by a rise along the axis; its summit reaches ~−2.4 km. Two magnetic profiles along segments 3 and 6 (Fig. 6a) are slightly clockwise rotated relative to the seafloor fabric. The magnetic anomalies are approximately symmetric in the E-W direction. We estimated a full spreading rate of 52,3 mm/a along the ESR3, and of 62 mm/a along the ESR6. The good correlation between magnetic and bathymetric profiles suggests a symmetric spreading rate (Fig. 6a). The velocity of subduction (Fig. 6a), calculated considering the kinematics of the hinge, increases from north (~77 mm/a) to south (~87 mm/a).

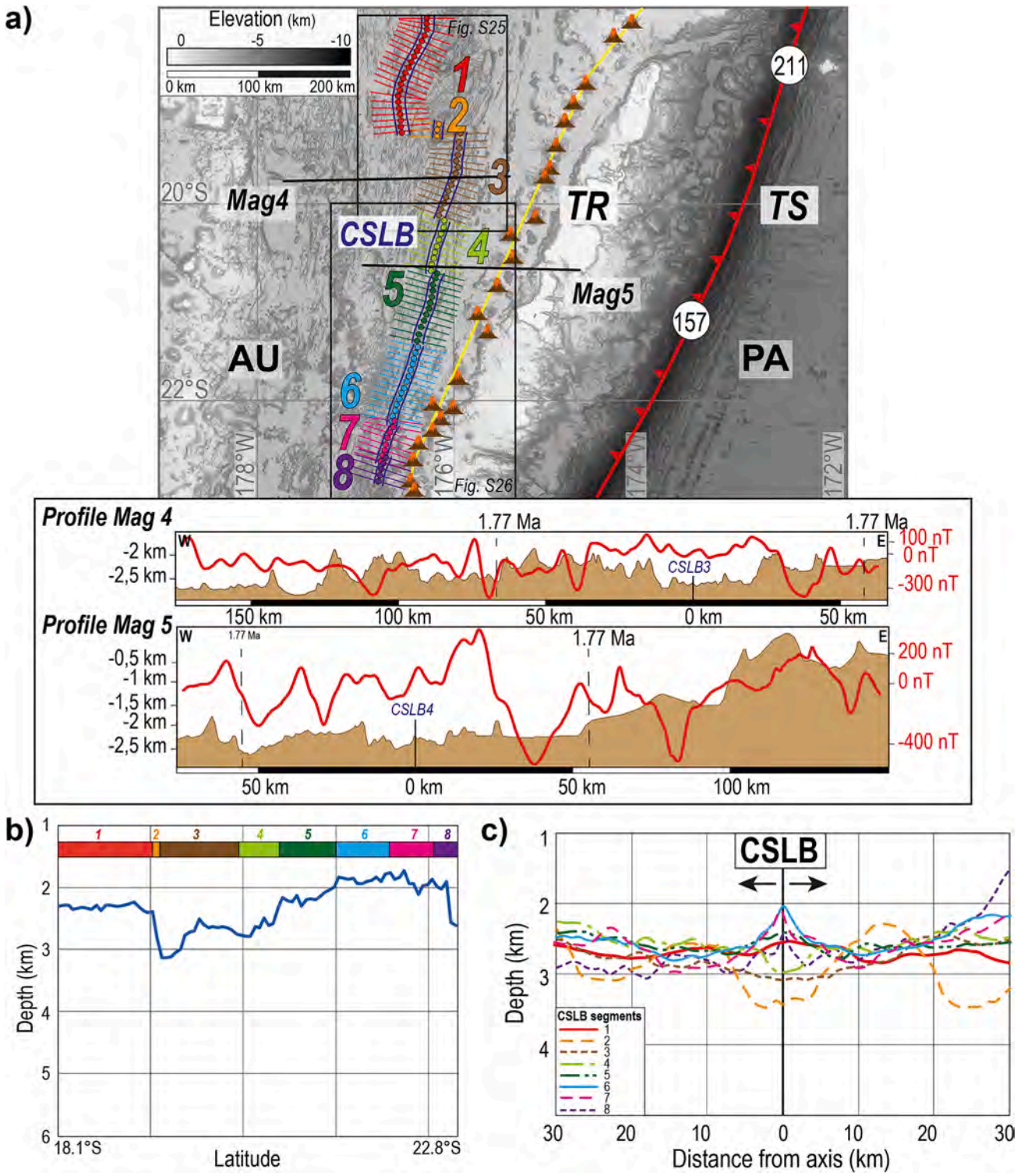

Fig. 7. a) Shaded grey relief image of the Lau Basin region. Colored dots and lines are respectively the 86 points and the bathymetric profiles identified and analyzed along the Central-Southern Lau Basin (CSLB) spreading centers. Red dots and lines: segment 1; Orange dots and lines: segment 2; Brown dots and lines: segment 3; Light green dots and lines: segment 4; Dark green dots and lines: segment 5; Light blue dots and lines: segment 6; Pink dots and lines: segment 7; Purple dots and lines: segment 8. Blue solid lines show the trend of the spreading segments. The black-solid lines crossing the CSLB segments 3 and 4 represent the bathymetric and magnetic profiles Mag4 and Mag5 shown in the lower part of the figure. White circles show the subduction rate (V_S) in mm/a measured according to Ficini et al. (2020). TR: Tonga Ridge; TS: Tonga Subduction. The yellow-solid line and the brown-orange triangles show active volcanism along the TR; the red-solid line with red triangles shows the TS. b) The blue-solid line in the diagram on the right shows the variation of the axial depth along the CSLB from north (18.1°S of latitude) to south (22.2°S of latitude). c) Depth/Distance from the axis diagram. Each profile represents an average of all bathymetric profiles obtained along each segment. The axis of the CSLB is in correspondence of the 0 km in the lower part of the diagram; the right parts of the profiles reflect the eastern flanks of the CSLB; the left parts of the profiles reflect the western flanks of the CSLB.

4.3. Central-Southern Lau Basin spreading center

The Central-Southern Lau Basin is characterized by eight segments from north (CSLB1; red dots) to south (CSLB8; violet dots) (Fig. 7a). We plotted the trend of the CSLB axial depth relative to the latitude in Fig. 7b (blue solid line of the depth/latitude diagram on the right); furthermore, the location and depth of each point identified along the CSLB spreading centers are shown in Figs. 7a, S25, and S26. Results show: a) the maximum axial depth is along segment 2, a short segment of spreading center located between the southern part of segment 1 and the northern part of the segment 3 (3.145 km at ~19.3°S of latitude); b) from segments 1 to 5 (if we exclude the second segment), the depth of the axis ranges between 3 and 2 km below sea level; c) the axial depth along the southern part of the Lau Basin, from segment 6 to 8, is <3000 m, reaching the minimum depth of 1732 m at ~22,2°S. The length of segments ranges from a minimum of 30 km (CSLB2) to a maximum of 130 km (CSLB1). The trend of all spreading segments is NE-SW, parallel to the trend of the Tonga Subduction (Fig. 7a). We carried out eighty-six 60-km-long bathymetric profiles perpendicular to the axis of the CSLB segments (Figs. 7a and S27 to S34), to show the variation of the bathymetry along the basin. The main range of depth for each segment, showing the variation of morphology in the first 30 km along their axis, is shown in Fig. 7c. Except for the CSLB2 segment, which shows a valley in correspondence with the axis (~3 km of depth; this is the deepest part along the entire CSLB segment system), all segments located in this region show either the absence of a valley (CSLB3 and CSLB4) or a rise that, in some cases, reaches <2 km below sea level. Furthermore, except for the second segment, there is no axial valley flanked by steep walls. Based on the magnetic data, we calculated a full spreading rate of 75 mm/a along the CSLB3 segment and 62 mm/a along the CSLB4 segment (Fig. 7a). Subduction rates along the Tonga Subduction, shown in Fig. 7a, increase from the central part (~59 mm/a) to the south (~62 mm/a).

5. Discussion

5.1. New insights on the oceanic spreading centers classification

The bathymetry and kinematics of the Mariana Spreading Center (MSC), the East Scotia Ridge (ESR), and the Central-Southern Lau Basin (CSLB), three back-arc spreading centers (BASCs) formed and developed in a similar geodynamic context, have been analyzed to improve the knowledge on oceanic geodiversity. In particular, the new bathymetric methods allowed to: 1) locate the axial point along the BASCs; 2) determine the variation of the BASCs' axial depth along their basins.

Based on the new location of the axial points, we refined the segments of microplate-plate boundaries with high resolution relative to those previously used in literature (e.g., Bird, 2003; Cuffaro and Jurdy, 2006; DeMets et al., 2010), such as the Philippine Sea – Mariana, Scotia – Sandwich, and Australia – Tonga divergent boundaries at MSC, ESR, and CSLB (Fig. 8). A comparison of the updated segments at the three examined BASCs with models by DeMets et al. (2010) is reported in Fig. 8. Evidence of refinement is especially shown in the northern part of the MSC (Fig. 8a.); whereas, in the southern part, the two digital models correlate better. A better fit is found for the ESR and CSLB (Fig. 8b and c), where the microplate boundaries by DeMets et al. (2010) stand mainly in the uncertainty band of the boundaries obtained here.

Furthermore, results of our bathymetric analyses also revealed differences in the depth of the back-arc spreading ridges, on average about 4.5, 3.5, and 2 km respectively at the MSC, ESR, and CSLB (Figs. 5b, 6b, and 7b). This bathymetric diversity is very common also along the axis of the global system of mid-ocean ridges (MORs), that generally are classified for "spreading rates" (Perfit and Chadwick, 1998; Small, 1998; Dick et al., 2003; Püthe and Gerya, 2014). The ultra-slow Gakkel Ridge (Fig. 1) (spreading rate < 12 mm/a) and the very-slow MORs (spreading rate between 12 and 20 mm/a), such as the South-West Indian Ridge (SWIR) (Fig. 1), show a rugged median valley which in places exceeds 2 km deep, with a depth at the axis of over 4,5 km (Fig. 9a; Dick et al., 2003). Slow MORs (spreading rate between 20 and 55 mm/a), such as

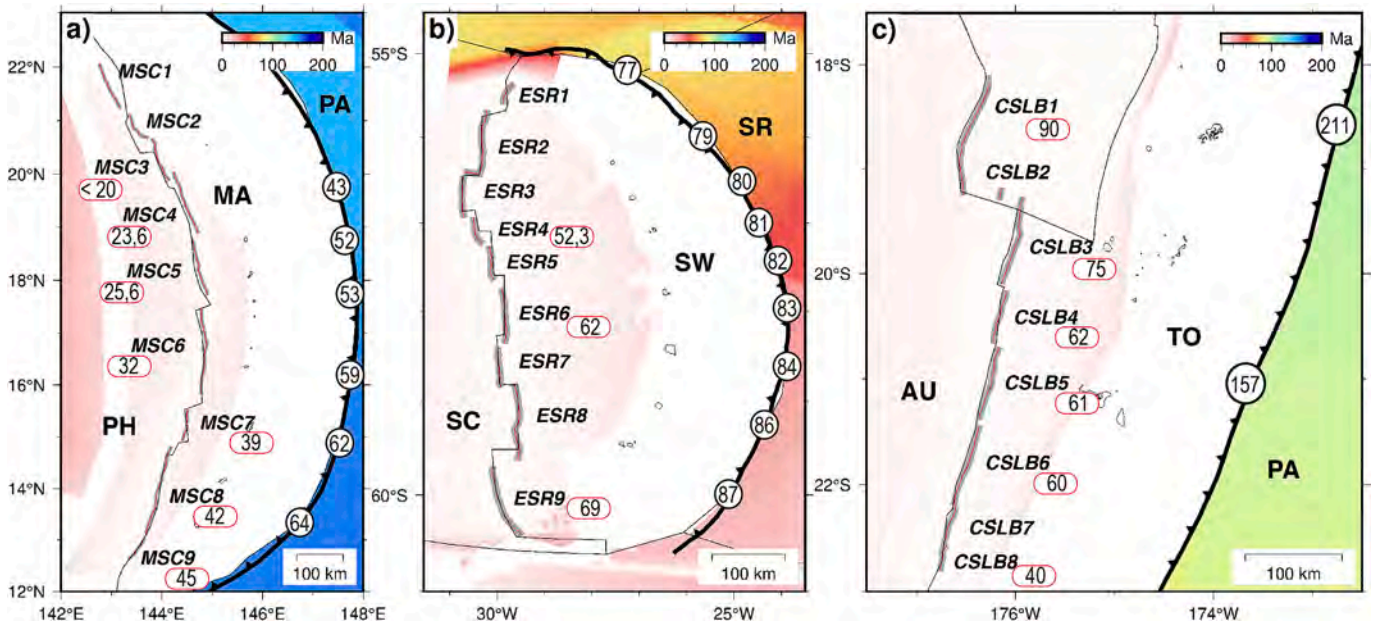

Fig. 8. Comparison between microplate boundaries by DeMets et al. (2010) (black lines) and refined segments of this study (red lines) at the three analyzed back-arc spreading centers (a) MSC, (b) ESR, and (c) CSLB, which characterize the Philippine Sea (PH) – Mariana (MA), the Scotia (SC) - South Sandwich SW) and the Australia (AU) – Tonga (TO) plate and microplate edges. Convergent plates at the MSC and CSLB are the Pacific (PA), whereas at ESR is the Sur (SR), respectively, according to DeMets et al. (2010). Sea floor crustal age is from by Müller et al. (2019) and Seton et al. (2020). The evidence of refinement is especially shown in the northern part, of the MSC (a), whereas in the southern part the two digital models better correlate. A better fit is found for the ESR and CSLB (b) and (c) where the microplate boundaries by DeMets et al. (2010) mostly stand in the 10-km uncertainty band of the boundaries here obtained (grey line). Values in the circles are the subduction velocities, and those in rounded rectangles are the full spreading rates.

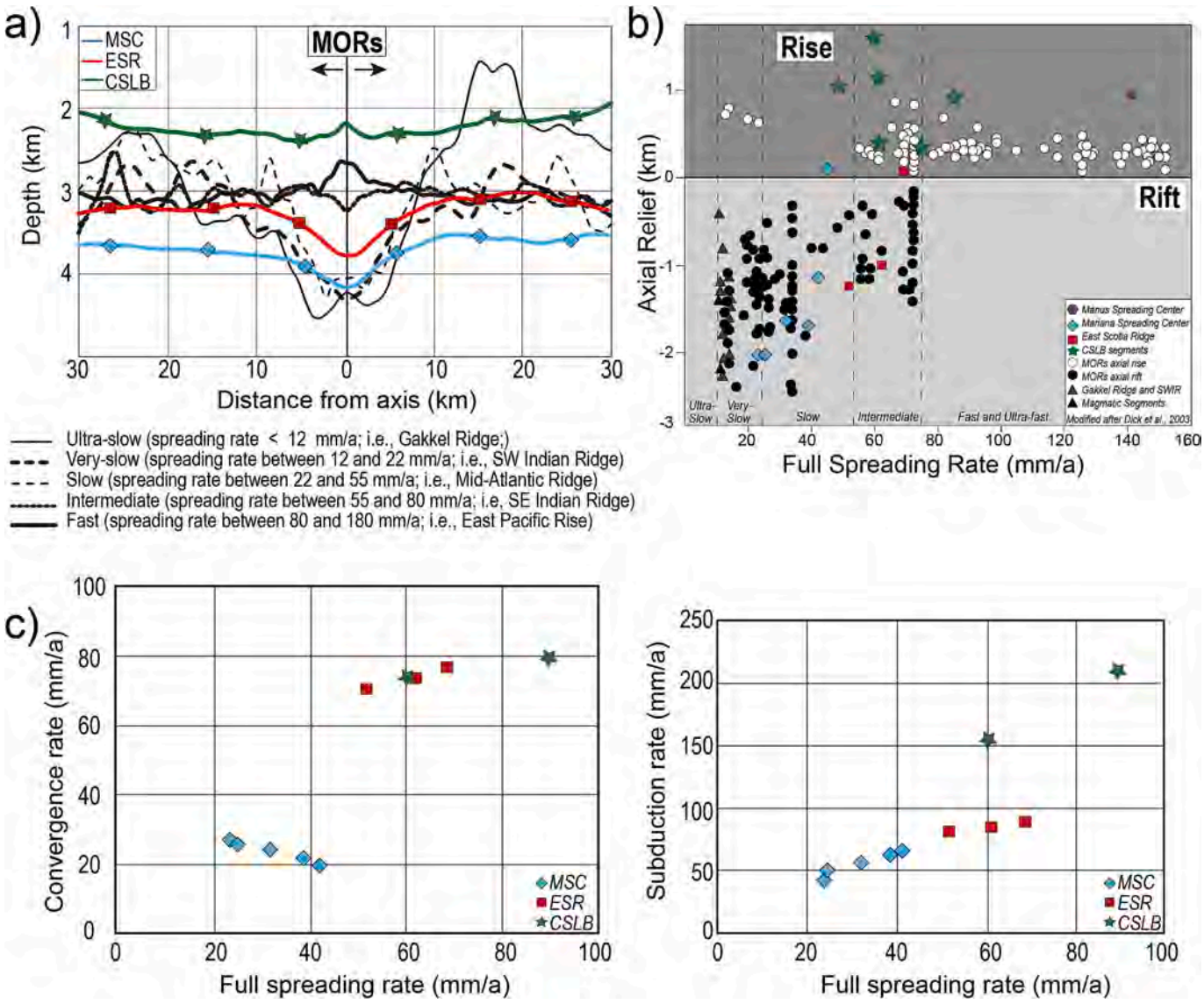

Fig. 9. a) Diagram depth/distance from axis showing the mean depth along the global system of MORs and along the MSC, ESR, and CSLB. The axis is located in correspondence with the 0 km in all the diagrams; the right parts of the profiles reflect the eastern part of the spreading centers; the left parts of the profiles reflect the western part of the spreading centers. b) Diagram axis depth/full spreading rate modified from Dick et al. (2003) including our data and data from literature along oceanic mature back-arc spreading centers. c) On the left, full spreading/convergence rates diagram along MSC, ESR, and CSLB; on the right, full spreading/subduction rates diagram along MSC, ESR, and CSLB. MSC: Mariana Spreading Center; ESR: East Scotia Ridge; CSLB: Central-Southern Lau Basin spreading centers.

the Mid-Atlantic Ridge (MAR) (Fig. 1), are characterized by rugged faulted block bathymetry and a 20–30 km wide, ~1–2 km deep axial median valley. The depth of slow MOR valleys ranges between 4 and 5 km (Fig. 9a; Escartín et al., 1999). Fast MORs (spreading rate between 75 and 160 mm/a), like the East Pacific Rise (EPR; Fig. 1), show a smoother topography and generally lack a median valley, having instead an axial high some 1–2 km wide. Their morphology is characterized by a large dome reaching between 2 and 1 km below sea level (Fig. 9a; Spiess et al., 1980). Finally, MORs with intermediate spreading rates (between 55 and 75 mm/a) can have either slow or fast type bathymetry (see the South-East Indian Ridge in Fig. 9a), and generally show an axial depth between 3 and 2 km below sea level.

Back-arc spreading centers (BASCs) are generally not included in these classifications (Kato et al., 2003; Taylor and Martinez, 2003; Hannington et al., 2005; Artemieva, 2023). However, our bathymetric data along the three examples of mature BASCs show a strong similarity between BASCs and MORs (Fig. 9a). The MSC morphology (light blue bathymetric profile in Fig. 9a) resembles that of the Mid-Atlantic Ridge, with a deep axial valley (from 5 to 4 km below sea level) bounded by steep flanks (see Supplementary Materials). Along the northern and central part of the MSC, the morphology is very similar to that of ultra-slow and slow MORs (the depth of the valley is >5 km), as already noted by Anderson et al. (2017), who stressed the similarities between MSC and MAR between 12.7° and 18.3° of latitude. In the southern part of the Mariana Trough, the segments MSC8 and MSC9 morphology is characterized by a long and continuous rise ranging between 3.6 and 3 km depth (see Fig. S3 and bathymetric profiles of Figs. S11 and S12). According to Taylor and Martinez (2003), there is a first-order difference concerning the depth of origin and geochemistry between lavas from the arc-region and those from central spreading axes. The presence of this axial high can be linked to a different mantle thermal or compositional anomaly due to its location near the volcanic arc (Taylor and Martinez, 2003). However, literature data also show several outliers along MORs because, in addition to spreading rates, other factors (e.g., magmatic supply, tectonic strain, composition, and thermal state of the mantle) can affect the morphology of MOR segments (Macdonald, 1982, 2001;

Rubin and Sinton, 2007). The spreading rate along the MSC (Fig. 8a) increases from 26 mm/a (full rate) in the north (~18°N; MCS5) to 45 mm/a in the south (~13,5°N; MCS8) according to GPS-derived data of Kato et al. (2003) and Anderson et al. (2017). Our magnetic data improved MSC spreading rates, calculating a value of 23,6 mm/a along segment 4 (Fig. 8a). Furthermore, based on Mag1 profile (Fig. 5a), we suggest a ridge jump of the MSC from the area north of segment 5 to segment 4; if we consider the MSC4 as the central median valley that generated the anomaly, the spreading became symmetric. The asymmetry of seafloor spreading along the MSC has also been highlighted in Yamazaki et al. (1993).

The ESR morphology (red bathymetric profile in Fig. 9a), with axial valley depths from 4 to 3 km below sea level, resembles the bathymetric range of intermediate MORs (Fig. 9a). The northern segment (ESR1) is the deepest; segments from ESR2 to ESR7 show similar morphology, with an axial valley depth ranging from 4 to 3 km; segment ESR8 does not show a valley and is located close to 3 km below sea level. The southern segment (ESR9) is the shallowest, and its first part shows a continuous axial rise. Based on two magnetic profiles (Fig. 6a), we suggested spreading rates of 52,3 mm/a along the ESR3 and of 62 mm/a along the ESR6 (Fig. 8b). This trend increasing southward correlates with a full spreading rate ranging from 59 to 68 mm/a of Smalley Jr. et al. (2007), and from 62 to 70 mm/a (Fig. 8b) of Livermore et al. (1995) and Thomas et al. (2003).

In the central part of the Lau Basin, the first segment (in literature, "Central Lau Spreading Center"; Martinez and Taylor, 2002) shows a morphological rise of ~2.5 km below sea level (Fig. 7 and Supplementary Figures), very similar to the fast East Pacific Rise (Fig. 9a). It is the longest and fastest segment of this area: according to Martinez and Taylor (2002), spreading rates here are 90–85 mm/a; according to Baxter et al. (2020), they are from 120 to 101 mm/a. The second segment (in literature, "Intermediate Lau Spreading Center"; Martinez and Taylor, 2003) is instead the shortest and deepest (Fig. 8 and Supplementary Figures). According to Taylor and Martinez (2003), it is a short segment of spreading located between two longer spreading centers. According to Baxter et al. (2020), it is a short transfer zone between two spreading segments. Based on its trend parallel to that of other spreading centers in this area, we consider the CSLB segment 2 as a short spreading center, given that transfer zones are generally perpendicular to spreading centers (Atwater and Macdonald, 1977). Segments from 3 to 5 (in literature, "East Lau Spreading Center"; Martinez and Taylor, 2003) are characterized neither by a rise nor by a valley (a subaxial magma chamber has not be detected by seismic profiles; Martinez and Taylor, 2002); however, the bathymetry continues to be very shallow, ranging from 2 to 3 km of depth (Fig. 7 and Supplementary Figures). We calculated a full spreading rate of 75 mm/a along the CLSB3 segment and 62 mm/a along the CSLB4 segment (Fig. 8c), lower than ~95 to ~60 mm/a calculated by Martinez and Taylor (2003). In the southern part of the Lau basin, segments from 6 to 8, corresponding in literature to the "Vala Fu Ridge", show a long and steady axial high at ~2.3 km of depth (Fig. 7 and Supplementary Materials), a magmatically robust ridge with a spreading rate from 60 to 40 mm/a (Martinez and Taylor, 2002; Fig. 8c).

Similarities of spreading rates and axial valley depths between BASCs and MOR are also revealed if we insert our data in the axial relief/full spreading rate diagram of Dick et al. (2003) (Fig. 9b). We also added values for the Manus Spreading Center along the Manus BAB, assuming a spreading rate of 140 mm/a (Taylor and Martinez, 2003) and an axial depth of ~2.2 km (Dyriw et al., 2021), revealing a strong correlation between axial relief and full spreading rates along all back-arc spreading centers, very similar to data correlations along mid-ocean ridges.

5.2. The kinematic contribution to back-arc spreading centers geodiversity

Driving mechanisms for spreading along back-arc spreading centers are linked to processes along subduction zones, their diversity, and kinematics, and the thermal state and composition of the sub-mantle (Sdrolias and Muller, 2006). Here, we discuss the geodiversity of the Mariana, South Sandwich, and Tonga Subductions in order to see how their geodynamic features influence the morphology and kinematics along Mariana Spreading Centers (MSC), the East Scotia Ridge (ESR), and the segments located in the Central-Southern Lau Basin (CSLB).

Seafloor crustal ages of the subducting plates range from 140 to 154 along the Mariana Subduction (MS), from 50 to 80 along the northern part of the South Sandwich Subduction (SSS), from 8 to 30 along the southern part of the SSS, and from 88 to 120 along the Tonga Subductions (Figs. 2–4 and 8). The convergence velocities (Figs. 2–4) range from 19 mm/a to 27 mm/a along Mariana, from 67 mm/a to 77 mm/a along South Sandwich, and from 75 mm/a to 80 mm/a along Tonga. The dips of the subducting slabs, at the point of maximum curvature shown in Figs. 2–4, are 77° at Mariana, 55° at South Sandwich, and 57° at Tonga. Subduction velocities range from 43 mm/a to 64 mm/a along MS, from 77 mm/a to 87 mm/a along SSS, and from 157 mm/a to 211 mm/a along TS (Figs. 5–7 and 8).

We plotted in Fig. 9c the spreading rates along the MSC, ESR, and CSLB versus the convergence (V_L, left panel), and subduction (V_S, right panel) rates measured along the related subduction zones, respectively. Data along the MSC show an inverse trend between spreading rates and convergence rates, which increase (from <20 to 45 mm/a) and decrease (from 27 to 19 mm/a) southward, respectively, whereas the subduction rate increases southward (from 43 to 64 mm/a). Otherwise, along the ESR, each of the spreading rates (from ~53 to 70 mm/a), the convergence rates (from 67 to 77 mm/a), and the subduction rates (from 77 to 87 mm/a) increase southward, whereas along the Central-Southern Lau Basin, the spreading rates (from ~90 to 40 mm/a), the convergence rates along the Tonga Subduction (from 80 to 75 mm/a), and the measured values of subduction rate (from 211 to 157 mm/a) decrease southward.

Retrieving data on the motion of a subduction hinge could be extremely complicated. According to the global analysis of Ficini et al. (2020), only one representative geodetic value was used to characterize the hinge velocity V_H. Local analyses (i.e., this study) need an increase in data resolution, including GPS points (Kato et al., 2003). Following this approach, we obtain a correlation between V_S and V_H, as this paper shows for the Mariana, South Sandwich, and Tonga Subductions. This implies that the hinge velocity could play a fundamental role in the subduction process, back-.arc basin evolution, and back-arc spreading center maturation degree. Ha et al. (2023) suggested that the formation of a BASC is influenced primarily by the motion of the subducting hinge, particularly in response to alterations in the slab geometry. Those authors also correlate the high variability of the Mariana slab dip with respect to the Sandwich and Tonga dips, stressing the importance of hinge motion at the back-arc basin of a subduction zone. Here, we obtained evidence of this important contribution at the MSC, where V_H has a significant role in producing a direct relation between V_S and spreading rates within the back-arc basin.

An interesting observation that is retrieved from our work is that some of the spreading centers (e.g., Mariana) are characterized by asymmetric opening while others are not. Although it would require specific and thorough dedicated work, we believe that observed different kinematics can also be related to mantle heterogeneities, which may produce partial sliding of lithospheric plates, plate motion changes (Cuffaro et al., 2008), and variable half-spreading rates along plate boundaries. Moreover, even though we only made our analyses on three case studies, we are confident that some relation could be found for all spreading centers in back-arc basins at their mature stage. This is also based on recent literature (e.g., Ha et al., 2023; Ficini et al., 2024), where the kinematics of the subducting plate, including that of the slab hinge, appear as a pillar for the deformation regime developed within the upper plate at subduction zones.

6. Conclusion

The morphology and kinematics of the Mariana Spreading Center (MSC), and the Central-Southern Lau Basin (CSLB) in the Pacific, and of the East Scotia Ridge (ESR) in the Southern Atlantic, all caused by extensional tectonics along ocean convergence, show evidence of geodiversity. The results of our bathymetric analyses revealed differences in the depth of the back-arc spreading ridges, on average about 4.5, 3.5, and 2 km respectively, at the MSC, ESR, and CSLB. Furthermore, the detailed description of the location of the axial point along oceanic mature back-arc spreading centers, with the proposed methods of this study, also contributes to the knowledge of high-resolution microplate-plate boundaries, with the analysis of magnetic profiles providing additional kinematic information along those boundaries with new full spreading rate data.

Despite the strong morphological and kinematic geodiversity, our results suggest that (1) the MSC resembles slow and ultra-slow mid-ocean ridges; (2) the ESR resembles intermediate mid-ocean ridges; (3) the CSLB resembles fast mid-ocean ridges; (4) kinematic modeling of subduction velocity along Mariana, South Sandwich, and Tonga, stresses the hinge contributions in the back-arc spreading rates.

This paper suggests that the geodiversity of the mature back-arc spreading centers, forming during different geodynamic processes along oceanic subduction zones, correlates perfectly with the geodiversity of the global mid-ocean ridge systems along divergent plate boundaries. Furthermore, this paper contributes to understanding how oceanic geodiversity is directly related to geodynamic processes, showing how hinge kinematics affects the relationship between convergence along subduction zones and spreading rates along back-arc spreading centers.

CRediT authorship contribution statement

C. Palmiotto: Writing – original draft, Visualization, Validation, Supervision, Methodology, Data curation, Conceptualization. **F. Muccini:** Writing – original draft, Methodology, Formal analysis, Data curation. **E. Ficini:** Writing – original draft, Software, Methodology, Formal analysis, Data curation. **M.F. Loreto:** Software, Methodology, Formal analysis, Data curation. **M. Cuffaro:** Writing – original draft, Visualization, Supervision, Methodology, Formal analysis, Data curation, Conceptualization.

Declaration of competing interest

The authors declare that they have no known competing financial interests or personal relationships that could have appeared to influence the work reported in this paper.

Acknowledgements

We warmly thank Enrico Bonatti (LDEO-Columbia University; Ismar-CNR) for reading the first draft of the paper and for his constructive suggestions. Comments by the two anonymous reviewers were useful to improve the manuscript. This study is co-funded by the ordinary contribution from authors' institutions.

Appendix A. Supplementary data

Supplementary data to this article can be found online at https://doi.org/10.1016/j.geomorph.2024.109466.

Data availability

Data will be made available on request.

References

Anderson, M.O., Chadwick Jr., W.W., Hannington, M.D., Merle, S.G., Resing, J.A., Baker, E.T., Butterfield, D.A., Walker, S.L., Augustin, N., 2017. Geological interpretation of volcanism and segmentation of the Mariana back-arc spreading center between 12.78°N and 18.38°N. Geochem. Geophys. Geosyst. 18, 2240–2274.
Anderson, R.N., 1975. Heat flow in the Mariana marginal basin. J. Geophys. Res. 80, 4043–4048.
Artemieva, I.M., 2023. Back-arc basins: a global view from geophysical synthesis and analysis. Earth Sci. Rev. 236, 104242.
Atwater, T., MacDonald, K.C., 1977. Are spreading centers perpendicular to their transform faults? Nature 270, 715–719.
Baker, E.T., German, C.R., 2004. On the global distribution of hydrothermal vent fields. In: German, C.R., Lin, J., Parson, L.M. (Eds.), Mid-ocean Ridges: Hydrothermal Interactions Between the Lithosphere and Oceans, Geophysical Monograph Series, 148. American Geophysical Union, pp. 245–266.
Baxter, A.T., Hannington, M.D., Stewart, M.S., Emberley, J.M., Brejer, K., Kratschell, A., Petersen, S., Brandl, P.A., Klischies, M., Mensing, R., Anderson, M.O., 2020. Shallow seismicity and the classification of structures in the Lau Back-Arc Basin. Geochem. Geophys. Geosyst. 21, e2020GC008924.
Bibee, L.D., Shor, G.G., Lu, R.S., 1980. Inter-arc spreading in the Mariana Trough. Mar. Geol. 35, 183–197.
Bird, P., 2003. An updated digital model of plate boundaries. Geochem. Geophys. Geosyst. 4.
Cande, S.C., Kent, D.V., 1995. Revised calibration of the geomagnetic polarity time scale for the Late Cretaceous and Cenozoic. J. Geophys. Res. 100, 6093–6095.
Chadwick Jr., W.W., Merle, S.G., Baker, E.T., Walker, S.L., Resing, J.A., Butterfield, D.A., Anderson, M.O., Baumberger, T., Bobbitt, A.M., 2018. A recent volcanic eruption discovered on the Central Mariana Back-Arc Spreading Center. Front. Earth Sci. 6, 172.
Crameri, F., Shepard, G.E., Heron, P.J., 2020. The misuse of colour in science communication. Nat. Commun. 11, 5444.
Cuffaro, M., Jurdy, D.M., 2006. Microplate motions in the hotspot reference frame. Terra Nova 18 (4), 276–281.
Cuffaro, M., Caputo, M., Doglioni, C., 2008. Plate subrotations. Tectonics 27, TC4007. https://doi.org/10.1029/2007TC002182.
DeMets, C., Gordon, R.G., Argus, D.F., 2010. Geologically current plate motions. Geophys. J. Int. 181, 1–80.
Dick, H.J.B., Lin, L., Schouten, H., 2003. An ultraslow-spreading class of ocean ridge. Nature 426, 405–412.
Doglioni, C., Carminati, E., Cuffaro, M., 2006. Simple kinematics of subduction zones. Int. Geol. Rev. 48, 479–493.
Doglioni, C., Carminati, E., Cuffaro, M., Scrocca, D., 2007. Subduction kinematics and dynamic constraints. Earth Sci. Rev. 83, 125–175.
Dyriw, N.J., Bryan, S.E., Richards, S.W., Parianos, J.M., Arculus, R.J., Gust, D.A., 2021. Morphotectonic analysis of the East Manus Basin, Papua New Guinea. Front. Earth Sci. 8, 596727.
Ekstrom, G., Nettles, M., Dziewonski, A.M., 2012. The global CMT project 2004-2010: centroid moment tensors for 13,017 earthquakes. Phys. Earth Planet. Inter. 200, 1–9.
Escartín, J., Cowie, P.A., Searle, R.C., Allerton, S., Mitchell, N.C., MacLeod, C.J., Slootweg, A.P., 1999. Quantifying tectonic strain and magmatic accretion at a slow spreading ridge segment, Mid-Atlantic Ridge, 29°N. J. Geophys. Res. 104, 10421–10437.
Ficini, E., Cuffaro, M., Doglioni, C., 2020. Asymmetric dynamics at subduction zones derived from plate kinematic constraints. Gondwana Res. 78, 110–125.
Ficini, E., Cuffaro, M., Doglioni, C., Gerya, T., 2024. Variable plate kinematics promotes changes in back-arc deformation regime along the north-eastern Eurasia plate boundary. Sci. Rep. 14, 7220. https://doi.org/10.1038/s41598-024-57890-6.
Fretwell, P., 2015. A Bathymetric and Topographic Compilation of the South Sandwich Island Volcanic Arc (Version None) [Data Set]. Polar Data Centre; British Antarctic Survey, Natural Environment Research Council, Cambridge, CB3 0ET, UK. https://doi.org/10.5285/b8143952-421c-4544-8437-58f339253d30.
Fretzdorff, S., Devey, C.W., Livermore, R.A., Leat, P.T., Stoffers, P., 2002. Petrogenesis of the back-arc East Scotia Ridge, South Atlantic Ocean. J. Petrol. 43, 1435–1467.
Fujiwara, T., Umino, S., Asada, M., Koike, Y., Kimoto, K., Kanamatsu, T., Okada, S., 2008. A submersible study of the Mariana Trough back-arc spreading center at 178N. JAMSTEC J. Deep Sea Res. 8, 61–73.
Gray, M., 2004. Geodiversity: Valuing and Conserving Abiotic Nature, 508p.. John Wiley & Sons, New York, NY, U.S.A. ISBN: 978-0470742150.
Ha, G., Montési, L.G.J., Zhu, W., 2023. Geometrical relations between slab dip and the location of volcanic arcs and back-arc spreading centers. Geochem. Geophys. Geosyst. 24, e2023GC010997.
Hannington, M.D., J. de Ronde, C.E., Petersen, S., 2005. Sea-floor tectonics and submarine hydrothermal systems. Econ. Geol. 100, 111–141.
Harris, P.T., Macmillan-Lawler, M., Rupp, J., Baker, E.K., 2014. Geomorphology of the oceans. Mar. Geol. 352, 4–24.
Hynes, A., Mott, J., 1985. On the causes of back-arc spreading. Geology 13, 387–389.
Karig, D.E., 1970. Ridges and basins of the Tonga-Kermadec island arc system. J. Geophys. Res. 75, 239–254.
Karig, D.E., 1971. Origin and development of marginal basins in the western Pacific. J. Geophys. Res. 76, 2542–2561.
Karig, D.E., Anderson, R.N., Bibee, L.D.T., 1978. Characteristics of back arc spreading in the Mariana Trough. J. Geophys. Res. 83, 1213–1226.
Kato, T., Beavan, J., Matsushima, T., Kotake, Y., Camacho, J.T., Nakao, S., 2003. Geodetic evidence of back-arc spreading in the Mariana Trough. Geophys. Res. Lett. 30, 1625.

Larter, R.D., Leat, P.T., 2003. Intra-oceanic subduction systems: tectonic and magmatic processes. Geol. Soc. Lond. Spec. Publ. 219, 1–17.
Leat, P.T., Pearce, J.A., Barker, P.F., Millar, I.L., Barry, T.L., Larter, R.D., 2004. Magmagenesis and mantle flow at a subducting slab edge: the South Sandwich arc-basin system. Earth Planet. Sci. Lett. 227, 17–35.
Livermore, R., Larter, R., Cunningham, A., Vanneste, L., Hunter, R.J., JR09 team, 1995. Hawaii-MR1 sonar survey of the east Scotia ridge. BRIDGE Newslett. 8, 51–53.
Macdonald, K.C., 1982. Mid-ocean ridges: fine scale tectonic, volcanic and hydrothermal processes within the plate boundary zone. Annu. Rev. Earth Planet. Sci. 10, 155–190.
Macdonald, K.C., 2001. Mid-ocean ridge tectonics, volcanism, and geomorphology. Encycl. Ocean Sci. 3, 1798–1813.
Maia, M.A.M., Castro, J.W.A., 2015. Methodological proposal for characterization of marine geodiversity in the South Atlantic: Vitória-Trinidade Ridge and adjacent areas, Southeast of Brasil. J. Integr. Coast. Zone Manag. 15, 293–309.
Malahoff, A., Feden, R.H., Fleming, H.S., 1982. Magnetic anomalie and tectonic fabric of marginal basins north of New Zealand. J. Geophys. Res. 87, 4109–4126.
Martinez, F., Taylor, B., 2002. Mantle wedge control on back-arc crustal accretion. Nature 416, 417–420.
Martinez, F., Fryer, P., Baker, N.A., Yamazaki, T., 1995. Evolution of backarc rifting: Mariana Trough, 20.8–24.8N. J. Geophys. Res. 100, 3807–3927.
Mendel, V., Munschy, M., Sauter, D., 2005. MODMAG, a MATLAB program to model marine magnetic anomalies. Comput. Geosci. 31, 589–597.
Müller, R.D., Roest, W.R., Royer, J.Y., Gahagan, L.M., Sclater, J.G., 1997. Digital isochrons of the world's ocean floor. J. Geophys. Res. 102, 3211–3214.
Müller, R.D., Zahirovic, S., Williams, S.E., Cannon, J., Seton, M., Bower, D.J., S.H. Bower, D.J., Tetley, M.G., Heine, C., Le Breton, E., Liu, S., Russell, S.H.J., Yang, T., Leonard, J., Gurnis, M., Russell, S.H., 2019. A global plate model including lithospheric deformation along major rifts and orogens since the Triassic. Tectonics 38 (6), 1884–1907.
NOAA (National Geophysical Data Center), 1977. Marine Trackline Geophysical Database. NOAA - National Centers for Environmental Information.
Palmiotto, C., Ficini, E., Loreto, M.F., Muccini, F., Cuffaro, M., 2022. Back-Arc spreading centers and superfast subduction: the case of the northern Lau Basin (SW Pacific Ocean). Geosciences 12, 50.
Parson, L.M., Wright, I.C., 1996. The Lau-Havre-Taupo back-arc basin: a southward propagating, multi-stage evolution from rifting to spreading. Tectonophysics 263, 1–22.
Perfit, M.R., Chadwick, W.W., 1998. Magmatism at mid-ocean ridges: constraints from volcanological and geochemical investigations. Geophys. Monogr. Am. Geophys. Union 106, 59–116.
Püthe, C., Gerya, T., 2014. Dependence of mid-ocean ridge morphology on spreading rate in numerical 3-D models. Gondwana Res. 25, 270–283.
Ribeiro, J.M., Stern, R.J., Martinez, F., Woodhead, J., Chen, M., Ohara, Y., 2017. Asthenospheric outflow from the shrinking Philippine Sea Plate: evidence from Hf-Nd isotopes of southern Mariana lavas. Earth Planet. Sci. Lett. 478, 258–271.
Rubin, K.H., Sinton, J.M., 2007. Inferences on mid-ocean ridge thermal and magmatic structure from MORB compositions. Earth Planet. Sci. Lett. 260, 257–276.
Sdrolias, M., Muller, R.D., 2006. Controls on back-arc basin formation. Geochem. Geophys. Geosyst. 7, 1–40.
Seijmonsbergen, A.C., Valentijn, S., Westerhof, L., Rijsdijk, K.F., 2022. Exploring ocean floor geodiversity in relation to mineral resources in the Southwest Pacific Ocean. Resources 11, 60.
Seton, M., Müller, R.D., Zahirovic, S., Williams, S., Wright, N., Cannon, J., Whittaker, J., Matthews, K., McGirr, R., 2020. A global dataset of present-day oceanic crustal age and seafloor spreading parameters. Geochem. Geophys. Geosyst. https://doi.org/10.1029/2020GC009214.
Small, C., 1998. In: Buck, W., Delaney, P.T., Karson, J.A., Lagabrielle, Y. (Eds.), Faulting and magmatism at mid-ocean ridges. American Geophysical Union, Washington, DC, USA, pp. 1–26, 1998.
Smalley Jr., R., Dalziel, W.D., Bevis, M.G., Kendrick, E., Stamps, D.S., King, E.C., Taylor, F.W., 2007. Scotia arc kinematics from GPS geodesy. Geophys. Res. Lett. 34, L21308.
Spiess, F.N., Macdonald, K.C., Atwater, T., Ballard, R., Carranza, A., Cordoba, D., Cox, C., Garcia, V.M., Francheteau, J., Guerrero, J., Hawkins, J., Haymon, R., Hessler, R., Juteau, T., Kastner, M., Larson, R., Luyendyk, B., Macdougall, J.D., Miller, S., Normark, W., Orcutt, J., Rangin, C., 1980. East pacific rise: hot springs and geophysical experiments. Science 207, 1421–1433.
Taylor, B., Martinez, F., 2003. Back-arc basin basalt systematics. Earth Planet. Sci. Lett. 210, 481–497.
Taylor, B., Zellmer, K., Martinez, F., Goodliffe, A., 1996. Sea-floor spreading in the Lau back-arc basin. Earth Planet. Sci. Lett. 144, 35–40.
Thébault, E., Finlay, C.C., Beggan, C.D., 2015. International geomagnetic reference field: the 12th generation. Earth Planets Space 67, 79.
Thomas, C., Livermore, R., Pollitz, F., 2003. Motion of the Scotia seaplates. Geophys. J. Int. 155, 789–804.
Tukiainen, H., Maliniemi, T., Alahahta, J., Hjort, J., Lindholm, M., Salminen, H., 2023. Quantifying alpha, beta and gamma geodiversity. Prog. Phys. Geogr. 47, 140–151.
Vine, F.J., Matthews, D.H., 1963. Magnetic anomalies over oceanic ridges. Nature 199, 949.
Wessel, P., Luis, J., Uieda, L., Scharroo, R., Wobbe, F., Smith, W., Tian, D., 2019. The generic mapping tools version 6. Geochem. Geophys. Geosyst. 20 (11), 5556–5564.
Yamazaki, T., Murakami, F., Saito, E., 1993. Mode of seafloor spreading in the northern Mariana Trough. Tectonophysics 221, 207–222.
Yan, Q., Shi, X., Yuan, L., Yan, S., Liu, Z., 2022. Tectono-magmatic evolution of the Philippine Sea Plate: a review. Geosyst. Geoenviron. 1, 100018.